The Astrophysical Journal Supplement Series, 172:720–731, 2007 October

LOW-FREQUENCY BEHAVIOR OF TURBULENCE FLUCTUATIONS AT MOUNT WILSON OBSERVATORY

Albert Wheelon, Nicholas Short, and Charles H. Townes
Space Sciences Laboratory, University of California, Berkeley, CA 94720; oxcart@cox.net
Received 2006 December 19; accepted 2007 April 14

ABSTRACT

Measurements and analysis of large-scale turbulent irregularities in the atmosphere are reported. Results were obtained from precision measurement of atmospheric temperature fluctuations at 24 and 70 feet above ground for a variety of wind velocities at the Mount Wilson Observatory. Measurements were made as wind blew air past detectors, at frequencies of 0.01–10 Hz, corresponding to distances in the atmosphere between about 1 and 250 m. Analysis shows that large-scale turbulences fit the Greenwood-Tarazano model well, and notably better than the von Karman model of turbulence.

Subject headings: atmospheric effects — techniques: interferometric — turbulence

1. INTRODUCTION

Fluctuations in the atmosphere of refractive index for optical and infrared wavelengths are associated largely with random temperature variations, and these irregularities impose fundamental difficulties on astronomical observations (see Appendix A). A good deal of effort has therefore been invested in measuring the characteristics of these random eddies and how their effects may be minimized. A different reason to study them comes from atmospheric science and interest in understanding how turbulent flow is generated in the troposphere. The two interests necessarily merge since temperature is a scalar quantity that is both created and moved about by turbulent velocity components.

One can measure temperature fluctuations in the atmospheric boundary layer directly using tower-mounted sensors. Such measurements have been made in the past. A pioneering program in the USSR made simultaneous tower and airborne measurements using identical sensors (Tsvang 1963). The aircraft flew a level path into the wind at an altitude of 70 m near the tower. This was the same height as the temperature and wind vector sensors mounted on the tower. Because the aircraft speed was more than 10 times the ambient wind speed, the irregularities appeared to be frozen during its transit. The aircraft data thus provided a snapshot of the eddies along a line at 70 m. By contrast, the tower readings changed stochastically with time as the wind carried the eddies past the sensor and as they evolved in response to turbulent velocity components. Comparisons of the two records showed that their power spectra were remarkably similar. This seemed to validate the Taylor hypothesis, which posits that the irregularities are frozen and carried past a sensor at constant speed. On the other hand, this agreement was limited to regions of the spectrum that are dominated by the inertial range of the turbulence.

In the succeeding years, temperature sensors have become more accurate, more sensitive, and provide faster response times. In addition, powerful data processing techniques have been developed that can now run on personal computers.

Our measurement program on Mount Wilson has exploited this progress and probed the high-frequency portions of temperature fluctuation spectra with some precision (Short et al. 2003). Interpretation of such data in terms of turbulence models must be done carefully. The structure of atmospheric irregularities requires a three-dimensional description. We use a small array of sensors, each of which provides a one-dimensional time series that is created as the wind blows the eddies past an observation point and as they are rearranged by turbulence. Our basic approach is to exploit the Taylor hypothesis, but to also use a small array of sensors and to establish bounds on results that reflect the limitations of this assumption.

At frequencies above approximately 0.1 Hz, the temperature spectrum is influenced primarily by small eddies in the inertial range of turbulence. This is the region in which progressive subdivision dominates the process, and it is accurately described by Kolmogorov's model of turbulent eddies. Our measurements simply confirm the spectral results expected from that model.

By contrast, the low-frequency components in our spectra behave quite differently. They are influenced primarily by large eddies in the hierarchy of turbulent fluctuations. Large eddies are the first to be created in the spontaneous transition from laminar to turbulent flow. This initiation of turbulent flow by ambient winds is not currently understood by hydrodynamicists. We hope to shed some light on it with the present measurements. Large-scale eddies are also important for the design and performance of interferometers as the baselines of these instruments increase (Wheelon 2001, p. 229). Experimental evidence indicates that the operation of current interferometers is influenced by these large eddies (Buscher et al. 1995; Davis et al. 1995). We exploit our low-frequency measurements to study turbulence that is relevant to such problems.

2. INSTRUMENTATION

Some temperature fluctuation measurements at the Mount Wilson Observatory by the Infrared Spatial Interferometer (ISI) group have already been reported (Short et al. 2003). The measurements relied on temperature sensors mounted on two telescoping masts that could reach to a height of 70 feet when fully extended. Five identical temperature sensors were mounted on each mast. When the masts were fully extended the five sensors provided readings every 15 feet at heights of 9, 24, 39, 54, and 70 feet. All observations were thus made in the boundary layer of the atmosphere.

An anemometer was installed at the top of one mast. Its readings represented most accurately the wind speed conditions for the uppermost temperature sensor, but were assumed to approximate the speed at lower heights. The individual temperature sensors were Type E style 2 thermocouples made by the Omega Company (model CO2-E). These provided data at fluctuation frequencies up to about 25 Hz. Five hundred seconds of a typical time series from one of these sensors is reproduced in Figure 1.

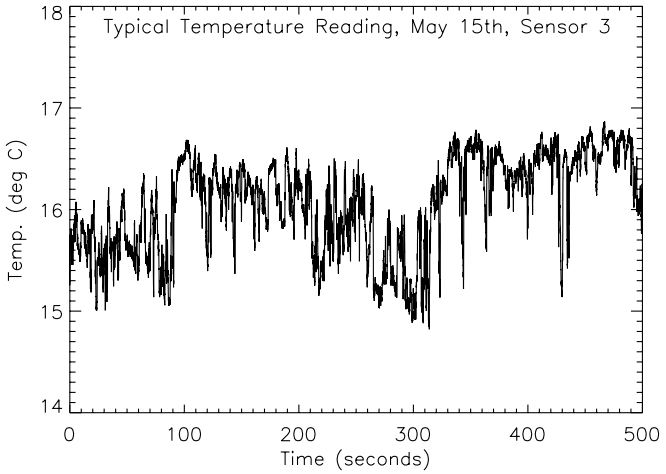

FIG. 1.—Atmospheric temperature fluctuations measured by a thermocouple over 500 s.

Such records provided power spectra of the temperature fluctuations, using the data processing approach described in the next section. The response time of the thermocouples is an important consideration in this process and was measured in our laboratory. The thermocouples were found to have response times ranging from 65 to 150 ms, depending primarily on the wind speed. The measured spectrum of temperature fluctuations $\overline{W_T(\omega)}$ was therefore expressed in terms of the true spectrum and the response time r_t of the detector by the following relationship:

$$\overline{W_T(\omega)} = W_T(\omega)\frac{1}{1+(\omega r_t)^2}. \quad (1)$$

3. DATA PROCESSING

The measurements taken at 24 and 70 feet above ground level were organized into 180 segments for each sensor. Each segment was about 22 minutes long and contained 2^{15} individual temperature readings. The individual segments were tagged with the average wind speed measured during the data intervals. Fourier transforms of these time series were then calculated that provided 180 individual power spectra for each sensor. These spectra were binned into seven wind speed ranges, as summarized in Table 1.

Some portions of each spectrum were eliminated. Noise and equipment tests with our system suggested that we ignore frequency components below 0.008 Hz since they probably did not represent atmospheric density fluctuations (see also Appendix B2). Spectral components above 10 Hz were also dropped because they represented unwanted signals or the inherent noise floor of our equipment. In addition, a small number of points in each spectrum were eliminated by visual inspection. These points appeared as peaks in the frequency range $\nu < 10$ Hz and were identified with unwanted electrical signals.

All of the edited spectra in a given wind speed bin were then averaged together. This averaging was done so that the resulting points would appear equally spaced on a logarithmic frequency scale. The process generated 145 spectrum values in the range $0.008 \text{ Hz} < \nu < 10$ Hz. The end result was a composite spectrum for each sensor and each wind-speed bin. These spectra provided the basis against which the theoretical models subsequently described were compared.

4. THEORETICAL FRAMEWORK

The temperature fluctuations measured were primarily generated by turbulence in the atmospheric boundary layer. Theoretical and experimental studies of these random movements (Batchelor 1953) provide the framework for analyzing our measurements. Turbulent velocities induced in the atmosphere are stochastic functions of time and position. This means that one must focus on their moments and correlations, which are represented by ensemble averages taken over all possible configurations of the atmosphere.

TABLE 1
NUMBER OF SPECTRA IN EACH WIND SPEED RANGE

Wind Speed (m s^{-1})	No. of Spectra
0.0–1.0	27
1.0–2.0	47
2.0–3.0	33
3.0–4.0	20
4.0–5.0	26
5.0–6.0	17
6.0–7.0	10

NOTE.—All individual spectra within each wind speed bin were averaged together to produce seven composite spectra for each sensor.

Similar ensemble averages describe passive scalar quantities that are created and transported by turbulent velocity components. Water vapor and temperature fluctuations are such scalars. Since the mean value of temperature fluctuations δT is chosen to be zero, the most important moment for our purposes is the temporal covariance,

$$\langle \delta T(\boldsymbol{r},\ t)\delta T(\boldsymbol{r},\ t+\tau)\rangle. \quad (2)$$

We must approach this average by first considering the spatial covariance of temperature fluctuations measured simultaneously at separated points,

$$\langle \delta T(\boldsymbol{r},\ t)\delta T(\boldsymbol{r}+\boldsymbol{\rho},\ t)\rangle, \quad (3)$$

where $\boldsymbol{\rho}$ is the vector separation between two sensors. Experience has shown that it is best to work with the three-dimensional wavenumber Fourier transform of the spatial covariance,

$$\langle \delta T(\boldsymbol{r},\ t)\delta T(\boldsymbol{r}+\boldsymbol{\rho},\ t)\rangle = \int \Phi_T(\boldsymbol{\kappa})e^{i\boldsymbol{\kappa}\cdot\boldsymbol{\rho}}\,d^3\kappa. \quad (4)$$

Temperature fluctuations are completely characterized by the wavenumber spectrum $\Phi_T(\boldsymbol{\kappa})$ in this formulation.[1] It describes the hierarchy of eddies with decreasing size or increasing $\boldsymbol{\kappa}$ as illustrated in Figure 2. The scalar wavenumber $\kappa = 2\pi/\ell$ is the inverse scale size of the eddies at each stage in the decay process, where ℓ represents the length of a full sine-wave variation.

The basic concept of turbulence is that the ambient wind field contributes a small fraction of its kinetic energy to establish large random eddies of size L_0. The actual way in which this happens is not understood and remains a major challenge for hydrodynamicists. What we do know is that the large eddies rapidly break up into smaller and smaller eddies. This progressive subdivision proceeds until the original energy input is dissipated by atmospheric viscosity. That happens primarily at a small scale size $\ell_0 \approx 5$ mm.

[1] However, this description does not include the influence of intermittent structures in the atmosphere such as thermal plumes, an aspect of turbulent behavior that is still very poorly understood.

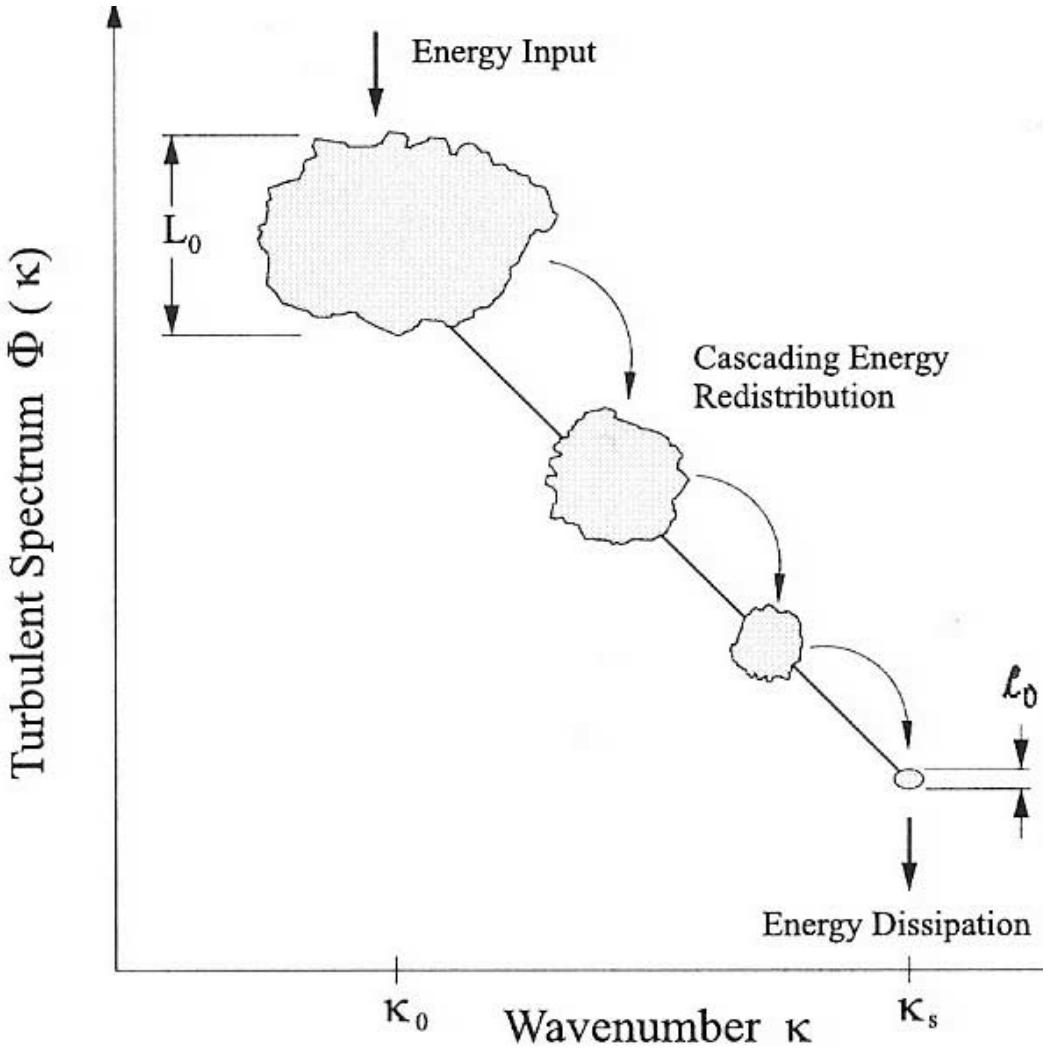

FIG. 2.—Conceptual description of the turbulent decay as it proceeds through an energy cascade process. The eddies divide into progressively smaller eddies until they finally disappear because of atmospheric viscosity.

The eddies are very nearly isotropic in the energy redistribution or inertial region. The spectrum depends only on the magnitude of the wavenumber vector $\kappa = |\boldsymbol{\kappa}|$ in this region. Using dimensional arguments, Kolmogorov showed that the spectrum in this subdivision cascade process is described by a simple power law (Kolmogorov 1941; Corrsin 1951; Obukhov 1949):

$$\Phi_T(\kappa) = \frac{0.033 C_T^2}{\kappa^{11/3}} \quad \text{for} \quad \frac{2\pi}{L_0} < \kappa < \frac{2\pi}{\ell_0}. \tag{5}$$

Here L_0 is the outer scale length that describes large eddies at the input stage. The inner scale length, l_0, identifies the eddy size at which energy is dissipated by viscosity. This expression is confirmed by a wide range of experiments. The inertial region exerts a strong influence on our measurements. However, the energy input range $\kappa < 2\pi/L_0$ also influences our data. We hope to use its effect to establish some features of the energy input region about which very little is now known.

The basic expression in equation (4) refers to simultaneous measurements made by separated sensors. The situation is different for most of our measurements. We have taken successive temperature readings with a single sensor and then converted them to power spectra. One can equate the two descriptions by assuming that the Taylor hypothesis is valid in our experiments. This approximation makes two important assumptions. It postulates that the relevant portion of the turbulent medium remains frozen during the measurement interval. It also assumes that one can ignore the turbulent component of wind velocity $\delta\boldsymbol{v}(\boldsymbol{r}, t)$ so that the wind velocity is constant and equal to $\boldsymbol{v}_0$ near the sensor. In combination, these assumptions imply that the entire air mass is transported horizontally past the sensor without being deformed. Applied to our situation, it means that the temporal variance for times t and $t + \tau$ should be identical to the spatial covariance for sensors separated by a vector

$$\boldsymbol{\rho} = \tau \boldsymbol{v}_0 \tag{6}$$

One can describe the temporal covariance by combining this equivalence with equation (4) to yield

$$\langle \delta T(\boldsymbol{r},\ t) \delta T(\boldsymbol{r},\ t + \tau) \rangle = \int \Phi_T(\boldsymbol{\kappa}) e^{i\tau \boldsymbol{\kappa} \cdot \boldsymbol{v}_0}\, d^3\kappa. \tag{7}$$

Transmission experiments made with laser beams show that turbulent irregularities are approximately isotropic and homogenous in the atmospheric boundary layer (Wheelon 2001, p. 78). This was confirmed in our temperature measurements that were reported earlier (Short et al. 2003). Using spherical wavenumber coordinates centered on the horizontal wind velocity, equation (7) can be simplified to

$$\langle \delta T(\boldsymbol{r},\ t)\delta T(\boldsymbol{r},\ t+\tau)\rangle = 4\pi \int_0^\infty \kappa^2 \Phi_T(\kappa)\left[\frac{\sin(\tau\kappa v_0)}{\tau\kappa v_0}\right] d\kappa. \tag{8}$$

The power spectrum and temporal covariance provide equivalent descriptions of the time series. They are connected to one another by a Fourier transform:

$$W_T(\omega) = \int_{-\infty}^{\infty} \langle \delta T(\boldsymbol{r},\ t)\delta T(\boldsymbol{r},\ t+\tau)\rangle e^{i\omega\tau}\, d\tau. \tag{9}$$

When we combine the last two equations and reverse the order of integration,

$$W_T(\omega) = \frac{8\pi}{v_0}\int_0^\infty \kappa\Phi_T(\kappa)\int_0^\infty \frac{d\tau}{\tau}\cos(\omega\tau)\sin(\kappa v_0\tau)\, d\kappa. \tag{10}$$

The integration over τ is discontinuous and given by

$$\int_0^\infty \cos(\omega\tau)\sin(\kappa v_0\tau)\frac{d\tau}{\tau} = \begin{cases} \dfrac{\pi}{2} & 0 < \omega < \kappa v_0, \\ 0 & \omega > \kappa v_0, \end{cases} \tag{11}$$

so that

$$W_T(\omega) = \frac{4\pi^2}{v_0}\int_{\omega/v_0}^\infty \kappa\Phi_T(\kappa)\, d\kappa. \tag{12}$$

This result will be used to make power spectrum predictions for two models of $\Phi_T(\kappa)$. These models have been proposed to describe the small wavenumber range $0 < \kappa < \kappa_0$, as equation (5) cannot. By comparing model predictions with our measurements, we hope to learn something about characteristics of the energy input region. In doing so, it is important to remember that the vital connection represented by equation (12) depends on the applicability of the Taylor hypothesis. That problem is examined carefully in Appendix B.

5. COMPARISON WITH THE VON KARMAN MODEL

The earliest attempts to describe the energy input region (Wheelon 2001, p. 38) simply ignored eddies with κ below the outer-scale wavenumber κ_0. The first attempt to characterize this region analytically was made by von Karman (von Karman 1948; Hinze 1975, p. 244). He proposed the following interpolation formula to describe fluid flow for $\kappa < \kappa_s = 2\pi/l_0$ using the structure constant C_T:

$$\Phi_T(\kappa) = \frac{0.033C_T^2}{\left(\kappa^2 + \kappa_0^2\right)^{11/6}} \text{ for } 0 < \kappa < \kappa_s \tag{13}$$

and found fair agreement with wind tunnel measurements. Note that this model reduces to the well-verified Kolmogorov form when $\kappa \gg \kappa_0$. The same expression has been widely used to describe atmospheric irregularities, even though the boundary conditions for the flow field are entirely different than those appropriate for a pipe or channel. This model is used primarily because it provided closed-form solutions for interesting problems.

One readily calculates the power spectrum using the expression by merging the model in equation (13) with equation (12):

$$W_T(\omega) = 0.7817C_T^2\frac{v_0^{2/3}}{\left(\omega^2 + \kappa_0^2 v_0^2\right)^{5/6}}. \tag{14}$$

The combination $\kappa_0 v_0$ is called the *"threshold frequency."* Substantially beyond this frequency the predicted spectrum falls off as

$$W_T(\omega) = 0.7817C_T^2\frac{v_0^{2/3}}{\omega^{5/3}} \text{ for } \omega \gg k_0 v_0, \tag{15}$$

and this behavior is consistently verified by temperature measurements. On the other hand, the power spectrum should approach a constant value for small frequencies if the von Karman model is correct:

$$W_T(\omega) = 0.7817C_T^2\frac{1}{v_0\kappa_0^{5/3}} \text{ for } \omega \ll \kappa_0 v_0. \tag{16}$$

These predictions need to be tested by examination of the entire range of frequencies to see if equation (14) matches the data. The measured power spectra were fitted to the following general form after the scintillation frequency was converted from rad s^{-1} to Hz using $\omega = 2\pi\nu$:

$$P(a,\ b,\ q,\ r_t;\ \nu) = a + \frac{b}{\left[q^2 + (2\pi\nu)^2\right]^{5/6}}\frac{1}{\left[1 + (2\pi\nu r_t)^2\right]}. \tag{17}$$

The exponent 5/6 is in agreement with the high-frequency portion of the spectrum that is verified by other experiments. We need to determine the parameters a, b, q, and r_t that best match the measured spectra for each wind speed. The parameter r_t represents the response time of the thermocouples and was also fitted because it can vary with wind speed.

The numerical technique for determining the parameters was straightforward. The difference between the averaged spectrum for each wind speed and the postulated form (eq. [17]) was calculated from the data for all 145 frequencies used. With this difference we computed the variance and summed over all points:

$$\chi^2 = \sum_{n=1}^{n=145}\frac{\left[W_T(\nu_n) - P(a,\ b,\ q,\ \tau;\ \nu_n)\right]^2}{\sigma_i^2}. \tag{18}$$

Here σ_i represents the standard deviation associated with each of the 145 points in the measured spectrum. The parameters a, b, q, and r_t were then allowed to vary randomly until a minimum value of χ^2 emerged. The parameter a was tightly constrained, since it represents the noise floor and could be estimated quite accurately from the high-frequency portion of the measured spectra.[2] The best values for the parameters fitted to the data taken at 70 feet are given in Table 2 for each speed bin. The minimum value of χ^2 is also included to indicate how good the fit was in each case. Comparable parameters for the sensor at 24 feet are given in Table 3.

[2] The interpretation of a as the constant noise floor was addressed in Short et al. (2003), in which confirming measurements were performed.

TABLE 2
VON KARMAN MODEL PARAMETERS

Wind Speed ($m\ s^{-1}$)	a ($deg^2\ Hz^{-1}$)	b ($deg^2\ Hz^{-1}\ rad^{5/3}\ s^{-5/3}$)	q ($rad\ s^{-1}$)	r_t (ms)	χ^2
0.0–1.0	0.0033	1.86	0.11	65	2.48
1.0–2.0	0.0027	2.73	0.15	65	0.93
2.0–3.0	0.0029	3.66	0.18	65	1.26
3.0–4.0	0.0034	6.35	0.25	65	1.20
4.0–5.0	0.0037	9.33	0.24	65	1.37
5.0.–6.0	0.0035	8.81	0.27	65	1.59
6.0–7.0	0.0033	7.99	0.17	50	3.43

NOTE.—Parameters for the von Karman model derived from temperature taken at 70 feet or 21.3 m.

In using the values obtained for various parameters several considerations are important. Because the wind speed was measured at the top of the mast, the indicated wind speeds represent conditions at the 70 foot sensor better than those at the 24 foot sensor. The fitting errors measured by χ^2 for the lower wind speeds are relatively large. That is expected because the Taylor hypothesis is not valid in those situations, as discussed in Appendix B. Values of χ^2 for the high speeds are also large, perhaps because the number of spectra available was relatively small. Accordingly, we do not use the first and last speed bins in further analysis.

The next step was to construct a best-fit theoretical curve for each wind speed. We did this by introducing our parameter solutions into the postulated form of equation (17). The theoretical curves had the general von Karman form but were specific to the conditions being measured on Mount Wilson. To see how well they tracked the measured data points, the resulting curves were overplotted on the corresponding averaged spectra. The comparisons for the sensor at 70 feet are reproduced in Figures 3 and 4 for both high and low wind speed conditions. These figures show that the von Karman model is quite accurate for frequencies above $\nu = 0.1$ Hz. That was to be expected since this range is controlled primarily by the Kolmogorov inertial range description.

The region below $\nu = 0.1$ Hz is the primary interest for our exploration. There the scatter of data points around the theoretical curves increases gradually as the frequency drops to the lower limit $\nu = 0.008$ Hz. The same behavior is apparent in the data taken at 24 feet that is presented in Figures 5 and 6. In both cases, it appears that the data points are bending over and they may be approaching a constant value, as predicted by equation (16). From these comparisons alone, however, we cannot be sure that this is the best description of the energy input region.

The von Karman model can be further tested using the presumed relationships between its physical parameters and the fitted

TABLE 3
VON KARMAN MODEL PARAMETERS

Wind Speed ($m\ s^{-1}$)	a ($deg^2\ Hz^{-1}$)	b ($deg^2\ Hz^{-1}\ rad^{5/3}\ s^{-5/3}$)	q ($rad\ s^{-1}$)	r_t (ms)	χ^2
0.0–1.0	0.0029	361.1	0.13	75	2.24
1.0–2.0	0.0028	529.3	0.13	75	1.36
2.0–3.0	0.0021	892.4	0.18	75	0.68
3.0–4.0	0.0037	715.8	0.16	75	1.05
4.0–5.0	0.0036	959.6	0.18	75	0.74
5.0–6.0	0.0024	1619.3	0.28	75	1.10
6.0–7.0	0.0023	705.9	0.29	75	3.31

NOTE.—Parameters for the von Karman model derived from temperature taken at 24 feet or 7.3 m.

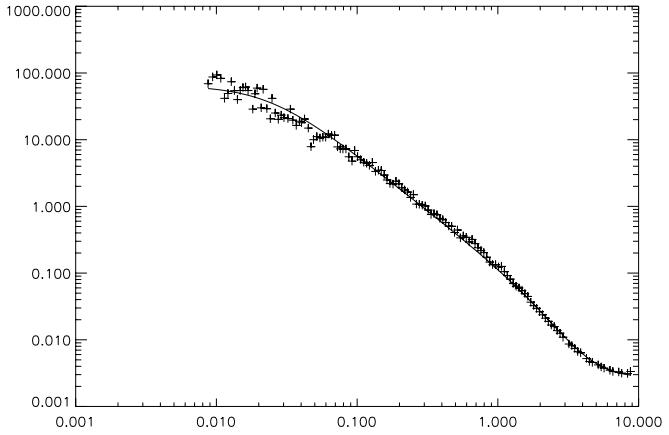

FIG. 3.—Power spectrum measured by the sensor at 70 feet. The horizontal axis represents frequency in Hz, while the vertical axis is in $deg^2\ Hz^{-1}$. These data reflect an average of 47 power spectra with wind speeds between 1 and 2 $m\ s^{-1}$. The best fit to the von Karman model is shown as the solid line.

constants presented in Tables 2 and 3. In doing so we establish a more stringent test for the model. The most telling examination results by comparing the denominator terms in equations (14) and (17),

$$q = \kappa_0 v_0, \tag{19}$$

where both quantities are measured in rad s^{-1}. In the von Karman model the parameter κ_0 is usually associated with the outer scale wavenumber and is inversely proportional to the outer scale length:

$$L_0 = \frac{2\pi}{\kappa_0}. \tag{20}$$

This means that we should be able to estimate L_0 from the fitted values for q using

$$L_0 = \frac{2\pi v_0}{q}. \tag{21}$$

From Tables 2 and 3 we notice that the values of q are *relatively* constant over the range of speeds that we encountered. This suggests that the horizontal outer-scale length is *roughly*

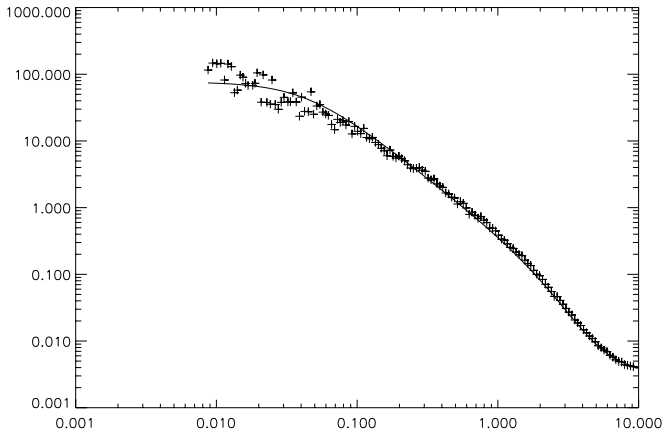

FIG. 4.—Power spectrum measured by the sensor at 70 feet. The horizontal axis represents frequency in Hz, while the vertical axis is in $deg^2\ Hz^{-1}$. These data reflect an average of 17 power spectra with wind speeds between 5 and 6 $m\ s^{-1}$. The best fit to the von Karman model is shown as the solid line.

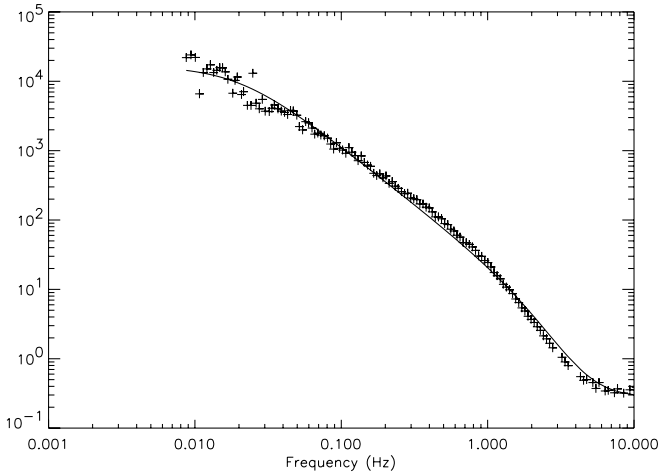

FIG. 5.—Power spectrum measured by the sensor at 24 feet. The horizontal axis represents frequency in Hz, while the vertical axis is in $\deg^2\ \mathrm{Hz}^{-1}$. These data reflect an average of 47 power spectra with wind speeds between 1 and 2 m s^{-1}. The best fit to the von Karman model is shown as the solid line.

proportional to wind speed. That relationship was discovered empirically in our earlier paper (Short et al. 2003).

We can take the relationship in equation (21) one step further. By using the fitted values for q we can estimate the outer-scale length as it is represented in the von Karman model for $\Phi_T(\kappa)$. Using the midpoint value in each wind-speed bin, one derives the values for L_0 shown in Table 4. In constructing this table we have omitted the lowest wind-speed bin because it probably does not satisfy the Taylor hypothesis. We have also omitted the highest wind-speed bin because it contains too few points and the estimated error is much larger than the other cases.

The values shown in Table 4 seem surprisingly large for two reasons. First, the outer scale length is usually assumed to be a fraction of the height (Tatarskii 1971, p. 77), and these values are much greater than either sensor height. Second, comparison of temperature fluctuations measured by sensors dislpaced horizontally suggested that the average horizontal eddy size was about 15 m (Short et al. 2003). Both estimates are much smaller than the derived values given above. There is a clear contradiction here, and it points to a fundamental problem with the von Karman

TABLE 4

OUTER SCALE LENGTH VALUES FOR VON KARMAN MODEL

Wind Speed (m s^{-1})	L_0 at 24 feet (m)	L_0 at 70 feet (m)
1.0–2.0	72	63
2.0–3.0	88	87
3.0–4.0	138	88
4.0–5.0	157	118
5.0–6.0	124	128

NOTE.—Values derived using eq. (21).

model. The small wavenumber portion of the spectrum defined by equation (15) is apparently flawed, at least when it is applied to the atmospheric boundary layer.

We can explore this issue in more detail by using the space-correlation measurements that were reported in our earlier paper (Short et al. 2003). The spatial correlation function that corresponds to the von Karman model is expressed in terms of a MacDonald function (Wheelon 2001, p. 42):

$$C(\rho) = 0.593(\kappa_0\rho)^{1/3}K_{1/3}(\kappa_0\rho). \tag{22}$$

This expression is plotted in Figure 11 below as a function of the dimensionless product of $\kappa_0\rho$. From that plot and the asymptotic version of this expression:

$$\lim_{\rho\Rightarrow\infty}[C(\rho)]\frac{0.743}{(\kappa_0\rho)^{1/6}}\exp(-\kappa_0\rho), \tag{23}$$

we see that the predicted correlation falls off slightly faster than an exponential for large values of the argument.

We measured the spatial correlation of temperature fluctuations on Mount Wilson, and the results were published in our earlier paper (Short et al. 2003). The horizontal correlation was measured between sensors at the same height on separated masts, but the data set provided in Figure 10 below was quite limited. On the other hand, simultaneous measurements between sensors deployed vertically on the same mast were plentiful and quite informative. The results for vertical separation between 5 and 18 m were provided in Figure 7 of our first paper and correspond to four different

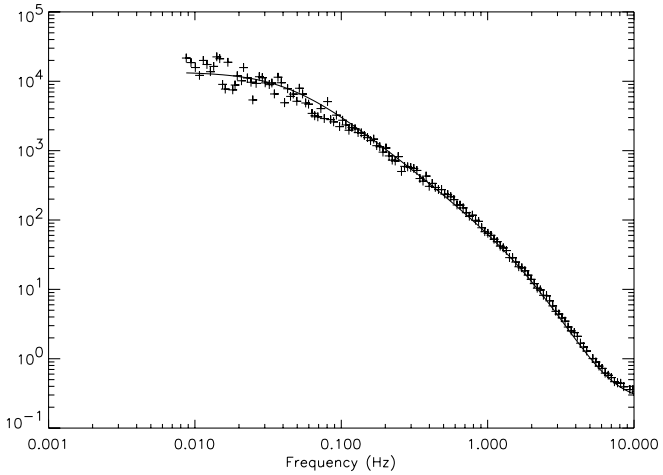

FIG. 6.—Power spectrum measured by the sensor at 24 feet. The horizontal axis represents frequency in Hz, while the vertical axis is in $\deg^2\ \mathrm{Hz}^{-1}$. These data reflect an average of 17 power spectra with wind speeds between 5 and 6 m s^{-1}. The best fit to the von Karman model is shown as the solid line.

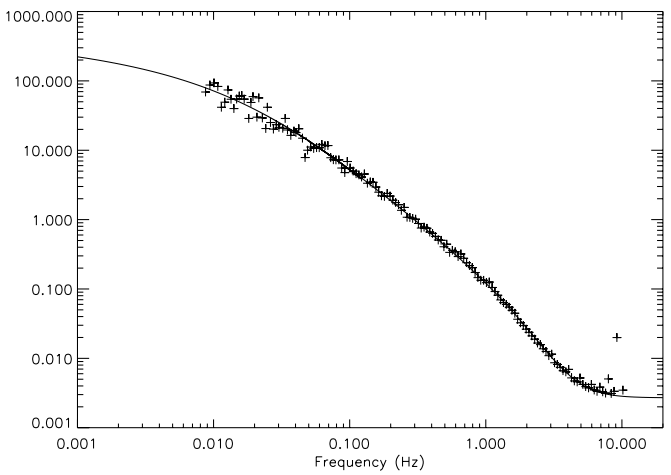

FIG. 7.—Power spectrum measured by the sensor at 70 feet. The horizontal axis represents frequency in Hz, while the vertical axis is in $\deg^2\ \mathrm{Hz}^{-1}$. These data reflect an average of 47 power spectra with wind speeds between 1 and 2 m s^{-1}. The best fit to the Greenwood-Tarazano model is shown as the solid line.

TABLE 5
GREENWOOD-TARAZANO MODEL PARAMETERS

Wind Speed (m s^{-1})	p (Hz^{-1})	d (deg^2 Hz^{-1})	r_t (ms)	e (deg^2 Hz^{-1})	χ^2
0.0–1.0	38.4	87.3	75	0.0033	3.90
1.0–2.0	40.9	119.9	74	0.0027	1.38
2.0–3.0	30.7	102.2	75	0.0029	0.83
3.0–4.0	19.0	83.6	79	0.0034	1.17
4.0–5.0	20.3	133.5	71	0.0037	0.78
5.0–6.0	16.8	95.1	74	0.0035	0.86
6.0–7.0	31.6	230.9	53	0.0033	2.18

NOTE.—Parameters in the Greenwood-Tarazano model derived from temperature data taken at 70 feet.

TABLE 6
GREENWOOD-TARAZANO MODEL PARAMETERS

Wind Speed (m s^{-1})	p (Hz^{-1})	d (deg^2 Hz^{-1})	r_t (ms)	e (deg^2 Hz^{-1})	χ^2
0.0–1.0	64.1	306.81	75	0.0030	2.20
1.0–2.0	58.2	390.18	75	0.0029	1.16
2.0–3.0	35.5	291.83	75	0.0024	0.74
3.0–4.0	43.0	323.80	75	0.0038	0.81
4.0–5.0	34.9	309.65	75	0.0038	0.56
5.0–6.0	18.3	185.09	75	0.0027	0.79
6.0–7.0	16.5	69.80	75	0.0023	1.75

NOTE.—Parameters in the Greenwood-Tarazano model derived from temperature data taken at 24 feet.

wind speed ranges. The measured vertical correlations fall gradually with separation distance and definitely do not agree with the exponential behavior predicted by equation (23).

It is interesting that progressively larger values of L_0 are required even to approximate our data. Those large values are roughly the same as those given in Table 4, which are based on power spectrum measurements. That makes sense because large separations correspond to large time delays according to the Taylor hypothesis. But large time delays give rise to low frequencies in the power spectrum, so both types of measurements are telling us the same thing. Our conclusion is that the von Karman model does not provide a decent description of the small wavenumber region for the turbulent spectrum $\Phi_T(\kappa)$ in the atmospheric boundary layer. That is a shame because it often leads to closed-form solutions for physical problems.

6. COMPARISON WITH THE GREENWOOD-TARAZANO MODEL

That brings us to the second model, with a good deal of hope. The Greenwood-Tarazano (GT) model of turbulence was established empirically (Greenwood & Tarazano 1974) using simultaneous temperature measurements made with nine identical temperature sensors. These sensors were deployed on a horizontal beam about one meter above the surface. Their locations were carefully chosen to provide 32 different spacings in the range of 4 cm to 6 m. The temperature fluctuations were 20 dB above the sensor noise level so the measurements were quite accurate. The results of many trials were compared with the spatial covariance expression

$$\langle \delta T(\boldsymbol{r},\ t)\delta T(\boldsymbol{r}+\boldsymbol{\rho},\ t)\rangle = 4\pi \int_0^\infty d\kappa\, \kappa^2 \left[\frac{\sin(\kappa\rho)}{\kappa\rho}\right]\phi_T(\kappa), \quad (24)$$

which is valid for the isotropic irregularities usually encountered near the surface. It was possible to identify a unique form that best summarized their measurements.

$$\phi_T(\kappa) = \frac{0.033 C_T^2}{(\kappa^2+\kappa\eta_0)^{11/6}} \text{ for } 0<\kappa<\kappa_s. \quad (25)$$

This expression transitions to the Kolmogorov model for large wavenumbers. However, it is quite different than the von Karman model for small wavenumbers, because it continues to rise as the eddies become larger and larger.

It is tempting to identify the parameter η_0 introduced here with κ_0 in the von Karman model since they both announce the beginning of the outer scale region at low wavenumbers. However, it is wrong to do so. The functional dependence on κ is quite different for the two models. The von Karman model goes flat as the wavenumber goes to zero, while the GT model continues to rise. This makes a significant difference for our experiments. Their respective parameters are likely to have quite different values. We therefore define a new outer scale length by the relation

$$D_0 = \frac{2\pi}{\eta_0}. \quad (26)$$

We want first to compare the predictions of the GT model with our power spectrum measurements. The predicted power spectrum is calculated by combining equations (12) and (25):

$$W_T(\omega) = 1.303 \frac{C_T}{v_0}(\eta_0)^{-5/3}\Lambda\left(\frac{\omega}{\eta_0 v_0}\right), \quad (27)$$

where a new function is defined by

$$\Lambda(x) = \int_x^\infty \frac{du}{u^{5/6}(1+u)^{11/6}}. \quad (28)$$

This function can be expressed analytically (see Appendix C), but it is simpler to compute it numerically. Like the von Karman result, it approaches a constant value for small frequencies:

$$W_T(\omega) = \frac{6.959 C_T^2}{v_0(\eta_0)^{5/3}} \text{ for } \omega \ll \eta_0 v_0. \quad (29)$$

Note that the numerical constant here is 9 times larger than the corresponding coefficient in equation (16) for comparable values of the parameters. The high-frequency behavior is identical to equation (15) since it is driven almost entirely by the Kolmogorov portion of the turbulence spectrum.

We used our numerical values for $\Lambda(x)$ to create the following trial function for the power spectrum:

$$Q(p,\ d,\ e,\ r_t,\ \nu) = e + \Lambda(\nu p)\frac{d}{1+(2\pi\nu r_t)^2}. \quad (30)$$

We have substituted $\omega = 2\pi\nu$ so that ν is measured in Hz. As before, we computed the difference between this function and the averaged spectra for each of the 145 points. Those results were used to evaluate the following variance taken over all the frequency values in each sample:

$$\chi^2 = \sum_{n=1}^{n=145} \frac{[W_T(\nu) - Q(p,\ d,\ e,\ r_t,\ \nu)]^2}{\sigma_i^2}. \quad (31)$$

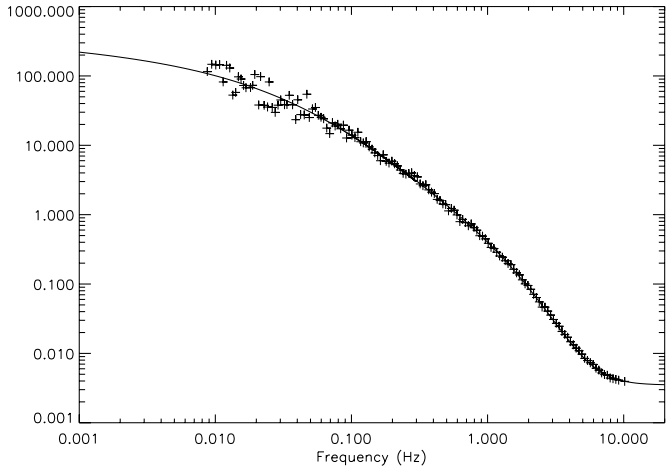

FIG. 8.—Power spectrum measured by the sensor at 70 feet. The horizontal axis represents frequency in Hz, while the vertical axis is in $\deg^2\ \mathrm{Hz}^{-1}$. These data reflect an average of 17 power spectra with wind speeds between 5 and 6 m s^{-1}. The best fit to the Greenwood-Tarazano model is shown as the solid line.

The variance σ_i was defined following equation (18). For each wind speed and location, the parameters p, d, e, and r_t were then varied until a minimum value of χ^2 was found. The best-fitting parameter values are presented in Tables 5 and 6. In using these results, we have tended to ignore the largest and smallest wind-speed bins for the reasons given above.

The actual data points measured at 70 feet on the mast are reproduced in Figures 7 and 8 for two wind-speed ranges. The averaged spectra for the same wind speed bins measured at 24 feet are presented in Figures 9 and 10. The corresponding fitted curves based on equation (30) that use the parameters from Tables 5 and 6 for each case are overplotted on the experimental data. The comparison of these fitted curves with the data points tells us how good the underlying turbulence spectrum model is. The spectrum curves based on the GT model fit the data remarkably well, even in the low-frequency region near $\nu = 0.01$ Hz. It is significant that the agreement here is considerably better than that obtained with the von Karman model.

We can further examine the validity of the trial expression in equation (30) by relating the fitted constants to the physical parameters in the derived power spectrum expression. We focus primarily on the combination $\eta_0 v_0$ that is related to the fitted constant p. Since p is measured in Hz^{-1} the outer-scale parameter becomes

$$D_0 = \frac{p v_0}{2\pi}. \tag{32}$$

From this relationship we can estimate the outer scale length for both sensor heights and the various wind-speed ranges. The results are presented in Table 7. These results are consistent with the estimates of eddy size given in our first paper. To the extent that the fitted values of p are constant, this means that the outer scale length should be proportional to the wind speed, as we found empirically.

We can perform a quantitative test using the spatial correlation measurements presented in Figure 7 of our earlier paper (Short et al. 2003). Those data points should be compared with the expression found by combining equations (24) and (25):

$$C(\rho) = \frac{0.749}{\rho\eta_0}\int_0^\infty \frac{\sin(x\rho\eta_0)}{(1+x)^{11/6}x^{5/6}}dx. \tag{33}$$

This integration can be expressed in terms of a Kummer function of the second kind (F):

$$C(\rho) = \frac{4.168}{\rho\eta_0}\Im\left[U\left(\frac{1}{6},\ -\frac{2}{3};\ -i\rho\eta_0\right)\right]. \tag{34}$$

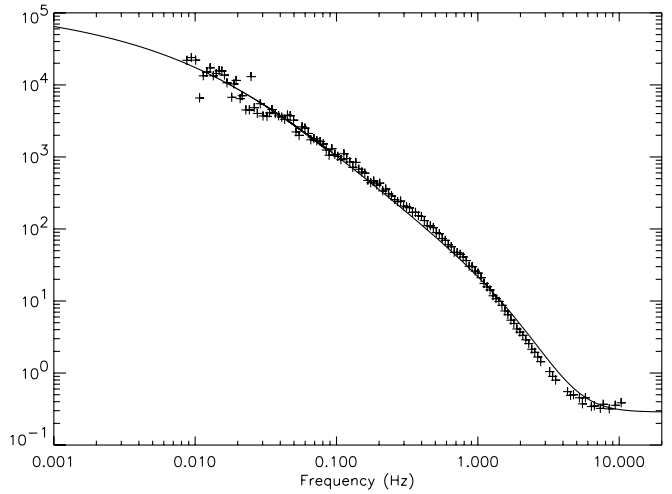

FIG. 9.—Power spectrum measured by the sensor at 24 feet. The horizontal axis represents frequency in Hz, while the vertical axis is in $\deg^2\ \mathrm{Hz}^{-1}$. These data reflect an average of 47 power spectra with wind speeds between 1 and 2 m s^{-1}. The best fit to the Greenwood-Tarazano model is shown as the solid line.

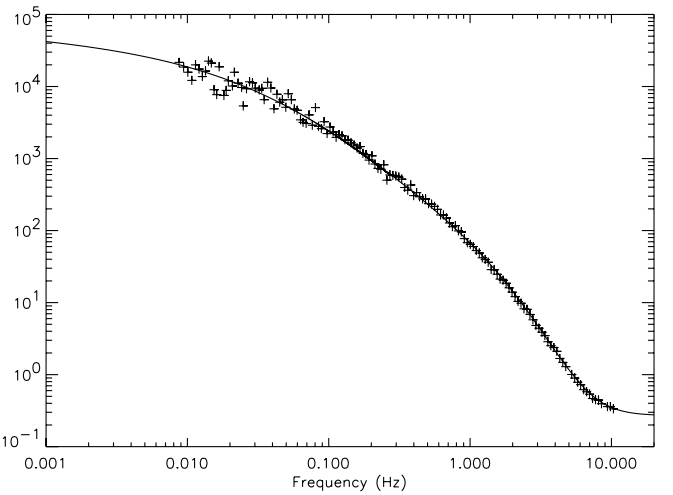

FIG. 10.—Power spectrum measured by the sensor at 24 feet. The horizontal axis represents frequency in Hz, while the vertical axis is in $\deg^2\ \mathrm{Hz}^{-1}$. These data reflect an average of 17 power spectra with wind speeds between 5 and 6 m s^{-1}. The best fit to the Greenwood-Tarazano model is shown as the solid line.

TABLE 7
OUTER SCALE LENGTH VALUES FOR GREENWOOD-TARAZANO MODEL

Wind Speed (m s^{-1})	D_0 at 24 feet (m)	D_0 at 70 feet (m)
1.0–2.0	10	14
2.0–3.0	12	14
3.0–4.0	10	24
4.0–5.0	15	25
5.0–6.0	15	16

NOTE.—Values derived using eq. (32).

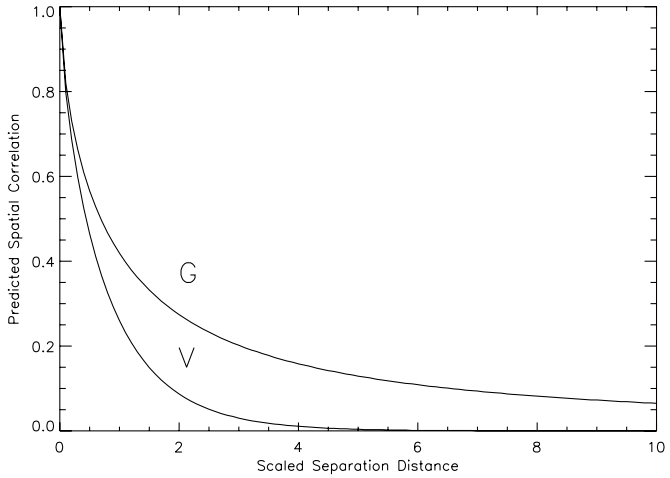

FIG. 11.—Plots of predicted spatial correlations between horizontally separated temperature sensors. The curve labeled V corresponds to the von Karman model and is a function of $\kappa_0\rho$. The curve labeled G is for the Greenwood-Tarazano model and is a function of $\eta_0\rho$. Note that κ_0 and η_0 have a different meaning and different values for the two models.

This expression is also plotted in Figure 11 as a function of the dimensionless combination $\rho\eta_0$. From that figure and the asymptotic form of this expression:

$$\lim_{\rho\Rightarrow\infty}[C(\rho)]=\frac{1.079}{(\rho\eta_0)^{7/6}}, \tag{35}$$

we see that the predicted spatial correlation should vary approximately as the inverse distance for large separations. That is quite different than the behavior of the von Karman model, but it is close to a reciprocal separation relationship suggested by our measurements.

To explore this matter more carefully, we exploited the tables that were used to plot $C(\rho)$ in Figure 11. Those numerical values were compared with the measured correlations at the four vertical spacings in the speed ranges 3–4 and 5–6 m s^{-1}. We find that a single value for η_0 matches these measured values quite nicely and leads to the following estimate via equation (26):

$$D_0 \simeq 28 \text{ m}. \tag{36}$$

This is not far from the value $D_0 = 25$ m that was derived in Table 7 for the same height and wind speed. The GT model therefore passes both the qualitative and the quantitative test.

7. GENERAL CONCLUSIONS

Our analysis has concentrated on exploring the outer scale region of turbulent irregularities in the atmospheric boundary layer. To do so, we relied on precision measurements of temperature fluctuations taken on Mount Wilson. These data streams were then used to establish their power spectra from 0.008 to 8.0 Hz for a variety of sensor heights and wind conditions. The low-frequency portion of these power spectra are strongly influenced by the large eddies that characterize the initiation of atmospheric turbulence.

We have compared our data with the predictions that are generated by the two leading models of turbulence that include the outer scale region: (1) the von Karman model (vK) and (2) the Greenwood-Tarazano (GT) model. We find that the vK prediction fits our low-frequency power spectrum data reasonably well. However, an even better fit is provided by the GT prediction. This preference is apparent in the data curves. It is even more evident in the smaller GT values of χ^2 in Tables 5 and 6, as compared to the vK values of χ^2 in Tables 2 and 3.

This preference becomes even stronger when one remembers that our estimate of χ^2 was based on all the points in the power spectrum. Since the two models are virtually identical for frequencies above 0.1 Hz, the substantial difference between their low-frequency agreements is masked by averaging over the entire frequency range. The GT model would therefore have been even more compelling than the vK model had we used only the low-frequency region in calculating χ^2.

In addition, we have found that the outer scale length values L_0 required by this fitting process are unreasonably large for the vK model. By contrast, the implied values for the outer scale parameter in the GT model given by D_0 are comparable to other estimates of the large eddy size. We recommend the GT model defined by equation (27) on the basis of these comparisons.

We have challenged the two models further. We compared the predictions for the spatial correlation with our data taken with vertically-displaced temperature sensors. The vK prediction falls exponentially with separation distance, whereas our data scales roughly as the inverse spacing. By contrast, the GT model accurately predicts an inverse scaling with separation. In this regard the GT is vastly superior to the vK model.

It is significant that the GT model was originally established empirically for temperature sensor spacings less than six meters. Our measurements now confirm its validity for separations as large as 18 m, and our power spectrum measurements confirm that conclusion. This extended verification may be helpful in the design and operation of optical and infrared interferometers.

Our conclusion is that the following turbulence model best describes temperature fluctuations in the atmospheric boundary layer, at least for the sensor heights and wind speed conditions we encountered:

$$\phi_T(\kappa)=\frac{0.033C_T^2}{[\kappa^2+(2\pi\kappa/D_0)]^{11/6}} \text{ for } 0\ll\kappa\ll\kappa_s. \tag{37}$$

We believe that the values for D_0 given in Table 7 describe the conditions on Mount Wilson. This conclusion is supported by our earlier observations that the turbulence there is approximately isotropic below 70 feet and that the Taylor hypothesis is valid for delay times less than 15 s.

The approximate values for the outer-scale of turbulence given by Table 7 indicate that the relative path length fluctuations for stellar light into two telescopes should not increase substantially for telescope separations larger than these values. This assumes that there are not localized temperature changes, vibrations, or motions that differ between the two telescopes as they are increasingly separated.

APPENDIX A

ANGULAR RESOLUTION FOR INTERFEROMETERS

The angular resolution $\delta\theta$ of an interferometer is limited by phase fluctuations and is approximately

$$\langle(\delta\theta)^2\rangle \approx \left(\frac{\lambda}{2\pi\rho}\right)^2\left\langle|\phi(r+\rho)-\phi(r)|^2\right\rangle, \tag{A1}$$

where ρ is the receiver separation, λ is the radiation wavelength, and $\phi(r)$ is the phase of radiation at an arbitrary position r. Phase fluctuations of the arriving signal are related to the refractive index variations δn integrated along the propagation paths through the atmosphere by

$$\delta\phi = \frac{\pi}{\lambda}\oint ds\,\delta n(s). \tag{A2}$$

Fluctuations in index of refraction depend on temperature variations according to

$$\delta n = \delta T\left[-77.6\frac{P}{T^2}\left(1+\frac{5.23\times 10^{-11}}{\lambda^2}\right)10^{-3}\right], \tag{A3}$$

where P is the pressure in bars, T the Kelvin temperature, and λ the wavelength in centimeters.

APPENDIX B

APPLICABILITY OF THE TAYLOR HYPOTHESIS

Our procedure for interpreting the power spectrum of temperature irregularities is only valid if the Taylor hypothesis is applicable to our experimental situation. We now examine that question. Specifically, the goal is to estimate the minimum frequency in the temperature spectrum that can be successfully measured by using this approximation. Two different phenomena can clearly undercut the Taylor hypothesis.

B1. WIND SPEED VARIATION

It is assumed that a constant wind bears the irregularities past the sensor, yet we know that wind speed and direction are not steady. Indeed, velocity fluctuations are the signature of turbulent behavior:

$$\boldsymbol{v} = \boldsymbol{v}_0 + \delta\boldsymbol{v}(\boldsymbol{r},\ t). \tag{B1}$$

This means that we must modify the relationship in equation (6) between time delay and equivalent spacing. When the time delay τ is relatively short the displacement caused by the velocity fluctuations can be approximated by

$$\rho = \tau\boldsymbol{v}_0 + \tau\delta\boldsymbol{v}(\boldsymbol{r},\ t), \tag{B2}$$

so long as the irregularities remain frozen in the neighborhood of the sensor. This reformulation of the Taylor hypothesis was introduced by Tatarskii, who called it the "locally frozen random medium approximation" (Tatarskii 1971, p. 127; Wheelon 2001, p. 246). In combination with the spatial covariance expression in equation (4), this means that

$$\langle\delta T(\boldsymbol{r},\ t)\delta T(\boldsymbol{r},\ t+\tau)\rangle = \int \Phi_T(\boldsymbol{\kappa})\exp\{i\tau\boldsymbol{\kappa}\cdot[\boldsymbol{v}_0+\delta\boldsymbol{v}(\boldsymbol{r},\ t)]\}\,d^3\kappa. \tag{B3}$$

This expression must be averaged over the ensemble of random velocity fluctuation components, which are stochastic functions of position and time. One can show that the fluctuations of temperature and velocity are uncorrelated if the fluid is incompressible (Wheelon 2001, p. 247), so that

$$\langle\delta T(\boldsymbol{r},\ t)\delta T(\boldsymbol{r},\ t+\tau)\rangle = \int \Phi_T(\kappa)\exp(i\tau\boldsymbol{\kappa}\cdot\boldsymbol{v}_0)\langle\exp[i\tau\boldsymbol{\kappa}\cdot\delta\boldsymbol{v}(\boldsymbol{r},\ t)]\rangle_{\delta v}d^3\kappa. \tag{B4}$$

The average over δv is recognized as the "characteristic function" of the velocity fluctuations. Turbulence theory shows one how to evaluate this special average, and one finds that

$$\langle\delta T(\boldsymbol{r},\ t)\delta T(\boldsymbol{r},\ t+\tau)\rangle = \int \Phi_T(\kappa)\exp(i\tau\boldsymbol{\kappa}\cdot\boldsymbol{v}_0)\exp\left(-\frac{1}{2}\kappa^2\tau^2\sigma_v^2\right)d^3\kappa, \tag{B5}$$

where σ_v is proportional to the rms velocity fluctuation:

$$\sigma_v^2 = \frac{2}{3}\left\langle|\delta\boldsymbol{v}|^2\right\rangle_{\delta v}. \tag{B6}$$

If the irregularities are isotropic, the temporal covariance becomes

$$\langle\delta T(\boldsymbol{r},\ t)\delta T(\boldsymbol{r},\ t+\tau)\rangle = 4\pi\int \kappa^2\Phi_T(\kappa)\left[\frac{\sin(\tau\kappa v_0)}{\tau\kappa v_0}\right]\exp\left(-\frac{1}{2}\kappa^2\tau^2\sigma_v^2\right)d\kappa. \tag{B7}$$

We can now establish an expression for the power spectrum of temperature variations that is valid for small random displacements. Using equation (B7) for the temporal covariance and combining it with the power spectrum in equation (10) we have

$$W_T(\omega) = \frac{8\pi}{v_0}\int_0^\infty \cos(\omega\tau)\,d\tau \int_0^\infty \kappa\Phi_T(\kappa)\frac{\sin(\tau\kappa v_0)}{\tau}\exp\left(-\frac{1}{2}\kappa^2\tau^2\sigma_v^2\right)d\kappa. \tag{B8}$$

It is useful to consider the steady wind case first. When there are no speed variations the power spectrum is described in terms of $\Phi_T(\kappa)$ by equation (12). One can differentiate that result with respect to ω to establish a direct connection between the measured power spectrum and the wavenumber spectrum of irregularities:

$$\Phi_T(\kappa) = \frac{v_0^3}{4\pi^2}\left[-\frac{1}{\omega}\frac{dW_T(\omega)}{d\omega}\right]_{\omega=\kappa v_0}. \tag{B9}$$

We can calculate the quantity on the right-hand side of equation (B9) by introducing the explicit expression for the power spectrum provided by equation (B8). Significantly, that expression includes the influence of wind-speed variations. It also depends on the power spectrum of temperature fluctuations. We introduce a new wavenumber symbol p in equation (B8) so as to avoid confusion with the argument κ of the spectrum on the left-hand side of equation (B9):

$$\Phi_T(\kappa) = \frac{2v_0^2}{\pi}\left[-\frac{1}{\omega}\frac{d}{d\omega}\int_0^\infty \cos(\tau\omega)\,d\tau \int_0^\infty p\Phi_T(p)\frac{\sin(\tau p v_0)}{\tau}\exp\left(-\frac{1}{2}\tau^2p^2\sigma_v^2\right)dp\right]_{\omega=\kappa v_0}. \tag{B10}$$

The plan is to complete both integrations and then see how closely the result matches $\Phi_T(\kappa)$ for various values of v_0 and δ_v. The frequency derivative and special value $\omega = \kappa v_0$ are easily taken. Reversing the order of integrations, we have

$$\Phi_T(\kappa) = \frac{2v_0}{\pi\kappa}\int_0^\infty p\Phi_T(p)\,dp \int_0^\infty \sin(\tau\kappa v_0)\sin(\tau p v_0)\exp\left(-\frac{1}{2}\tau^2p^2\sigma_v^2\right)d\tau. \tag{B11}$$

The integration over τ can be done analytically:

$$\int_0^\infty \sin(\tau\kappa v_0)\sin(\tau p v_0)\exp\left(-\frac{1}{2}\tau^2p^2\sigma_v^2\right)d\tau = \frac{\pi}{2}\frac{1}{p\sigma_v^2\sqrt{2\pi}}\left\{\exp\left[-\frac{1}{2}\left(\frac{v_0}{\sigma_v^2}\right)^2\left(\frac{p-k}{p}\right)^2\right] - \exp\left[-\frac{1}{2}\left(\frac{v_0}{\sigma_v^2}\right)^2\left(\frac{p+k}{p}\right)^2\right]\right\}. \tag{B12}$$

The second term does not contribute because neither p nor κ is ever negative:

$$\Phi_T(\kappa) = \frac{1}{\kappa}\int_0^\infty \Phi_T(p)dp\left\{\frac{v_0}{\sigma_v^2\sqrt{2\pi}}\exp\left[-\frac{1}{2}\left(\frac{v_0}{\sigma_v^2}\right)^2\left(\frac{p-k}{p}\right)^2\right]\right\}. \tag{B13}$$

Meteorological measurements show that the variable component σ_v^2 is only about 10% of the mean wind speed v_0, unless the ambient wind speed is itself very small. In the common case the square brackets is therefore well represented by the Dirac delta function (Wheelon 2001, p.420):

$$\lim_{\sigma_v^2/v_0\to 0}\left\{\frac{v_0}{\sigma_v^2\sqrt{2\pi}}\exp\left[-\frac{1}{2}\left(\frac{v_0}{\sigma_v^2}\right)^2\left(\frac{p-k}{p}\right)^2\right]\right\} = \delta\left(\frac{p-k}{p}\right) = p\delta(p-k). \tag{B14}$$

The general expression of equation (B9) therefore becomes

$$\Phi_T(\kappa) = \frac{1}{\kappa}\int_0^\infty p\Phi_T(p)\delta(p-k)\,dp. \tag{B15}$$

This relationship is satisfied identically provided only that the velocity fluctuations are small compared with the ambient wind. One can therefore use the Taylor hypothesis in almost all cases if the irregularities remain frozen.

One can generalize this conclusion to the case in which the displacements caused by the random velocity components are not small. In that case the equivalent spacing becomes

$$\boldsymbol{\rho} = \tau\boldsymbol{v}_0 + \int_0^\tau \delta\boldsymbol{v}(\boldsymbol{r},\ t). \tag{B16}$$

In this extension of the locally frozen random-medium approximation, one can show that the relationship in equation (B13) is still valid provided only that the wind speed fluctuations are modest compared to the ambient wind speed. We omit the details of this demonstration for lack of space.

B2. EVOLUTION OF THE TURBULENT EDDIES

The second part of the Taylor hypothesis assumes irregularities remain frozen during the measurement—at least in the neighborhood of the sensor. We have found only a few studies that address eddy evolution. The lifetimes of temperature irregularities in the inertial range was considered by Tatarskii (1971, p. 88). Using dimensional arguments, he showed that

$$T = \frac{\ell}{v(\ell)} = \frac{\ell^{2/3}}{\varepsilon^{1/3}}, \tag{B17}$$

where ε is the dissipation rate for the cascade process illustrated in Figure 2. This suggests that the Taylor hypothesis should be valid for single-point measurements if the influential eddies lie in the inertial region (Wheelon 2001, p. 242). On the other hand, this does not address the behavior of large eddies.

The situation is apparently quite different for large eddies that precede the inertial range. Detailed calculations based on the Navier-Stokes equations (Münch & Wheelon 1958) suggest that in the energy input region,

$$T = \frac{\ell}{2\pi v_0}. \tag{B18}$$

Moreover, these calculations indicate that the lifetimes for all eddies are influenced by the energy input region.

We judge that theoretical treatments of this question are too uncertain to provide reliable conclusions. Hence, we rely on experimental results (Short et al. 2003). Simultaneous measurements taken with sensors on adjacent masts suggested that passing eddies change their properties in about 15 s. It is partly for that reason we have ignored spectral data below $\nu_{\min} = 0.008$ Hz.

APPENDIX C

SMALL ARGUMENT EXPANSION FOR $\Lambda(\eta)$

The new function

$$\Lambda(\eta) = \int_{\eta}^{\infty} \frac{du}{u^{5/6}(u+1)^{11/6}} \tag{C1}$$

can be expressed in terms of the Gauss hypergeometric function by

$$\Lambda(\eta) = 5.342 - 6\eta^{1/6}\, {}_2F_1\left(\frac{11}{6},\ \frac{1}{6},\ \frac{5}{6},\ -\eta\right). \tag{C2}$$

The Gauss function can be replaced by unity for small values of the argument, yielding

$$\lim_{\eta \to 0}[\Lambda(\eta)] = 5.342 - 6\eta^{1/6}. \tag{C3}$$

REFERENCES

Batchelor, G. K. 1953, The Theory of Homogenous Turbulence (Cambridge: Cambridge Univ. Press)

Buscher, D. F., et al. 1995, Appl. Opt., 34, 1081

Corrsin, S. 1951, J. Appl. Phys., 22, 469

Davis, J., Lawson, P. R., Booth, A. J., Tango, W. J., & Thorvaldson, E. D. 1995, MNRAS, 273, L53

Greenwood, D. P., & Tarazano, D. O. 1974, A Proposed Form for the Atmospheric Microtemperature Spatial Spectrum in the Input Range, USAF Rome Air Development Center, Tech. Rep. RADC-TR-74-19

Hinze, J. O. 1975, Turbulence (2nd ed.; New York: McGraw-Hill)

Kolmogorov, A. N. 1941, Comptes Rendus (Doklady) de l'Academie des Sciences de l'URSS, 30, 301

Münch, G., & Wheelon, A. D. 1958, Phys. Fluids, 1, 462

Obukhov, A. M. 1949, Izvestiya Akademii Nauk SSSR, Seriya Geograficheskaya i Geofizicheskaya, 13, 58

Short, N., Fitelson, W., & Townes, C. 2003, ApJ, 599, 1469

Tatarskii, V. I. 1971, The Effects of the Turbulent Atmosphere on Wave Propogation (Springfield: Vistas Astron.)

Tsvang, L. R. 1963, Izvestiya Akademii Nauk SSSR, Seriya Geofizicheskaya, 10, 961

von Karman, T. 1948, Proc. National Academy of Science, 34, 530

Wheelon, A. D. 2001, Electromagnetic Scintillation. I. Geometrical Optics (Cambridge: Cambridge Univ. Press)